RESEARCH ARTICLE
SOLID EARTH: GEOELECTROMAGNETICS

Earth and Planetary Physics
9: 861–878, 2025
doi: 10.26464/epp2025018

Research on geomagnetic secular variation of China and surrounding areas based on the Geomagnetic Virtual Observatories

Jiang Li, and Bin Chen*

Institute of Geophysics, China Earthquake Administration, Beijing 100081, China

Key Points:

- We obtain three types of GVO series by using Swarm data, CSES data, and a combination of both data, respectively, then analyze the achievable accuracy of each.
- The GVO core field series matches well with ground observatory data, meeting the INTERMAGNET standard for quasi-definitive data of less than 5 nT.
- The one-month and four-month intervals GVO SV series that can achieve the highest accuracy are 2.03 nT/yr and 1.36 nT/yr, respectively.

Citation: Li, J., and Chen, B. (2025). Research on geomagnetic secular variation of China and surrounding areas based on the Geomagnetic Virtual Observatories. *Earth Planet. Phys.*, *9*(4), 861–878. http://doi.org/10.26464/epp2025018

Abstract: The Low Earth Orbit (LEO) geomagnetic satellites provide a large number of high-precision measurements, which are crucial for researching the Secular Variation (SV) of the geomagnetic field. We employ the combined constellation data from the Chinese Seismo-Electromagnet Satellite (CSES) and Swarm satellites to extract the SV in China and surrounding areas, based on the Geomagnetic Virtual Observatory (GVO) method. On this basis, we have developed two GVO products: the core field, and the SV series. The accuracies of these products are assessed using ground observatories measurements and geomagnetic field model. Moreover, the results indicate that the GVO products align well with the series from ground observatories and the CHAOS model. The majority of root-mean-square deviation (RMSE) values of the core field series are less than 5 nT, consistent with the INTERMAGNET standards for quasi-definitive data. In the GVO core field series, the maximum accuracy of one-month and four-month intervals are 2.24 nT and 1.16 nT, respectively. In the GVO SV series, the maximum accuracy of one-month and four-month intervals are 2.03 nT/yr and 1.36 nT/yr, respectively. The GVO SV series effectively capture geomagnetic jerks without losing temporal resolution comparing with the recording of ground observatories. We demonstrate that the GVO method serves as an effective and precise tool for extracting SV information of geomagnetic fields. In the GVO products, the RMSE of the horizontal component exceeds that of the vertical component, and the magnitude of RMSE deviation correlates with solar activity levels. With more and more geomagnetic satellites in orbit, we wish to use multi-constellation magnetic satellite data to assess the geomagnetic field more accurately.

Keywords: geomagnetic core field; secular variation; Geomagnetic Virtual Observatory; Swarm satellites; CSES satellite

1. Introduction

The geomagnetic field is one of the most significant geophysical fields of the Earth. According to the location of the field source, it can be divided into external and internal fields (Mandea and Olsen, 2006). The external field mainly includes the electrical current systems in the Earth's ionosphere and magnetosphere (Lu SK et al., 2016). The internal field consists mainly of the core field, which is generated by the process known as the geodynamo in the Earth's fluid outer core. The core field has a relatively long wavelength, and the dipole field dominates its spatial distribution. The temporal variation exhibits secular variation (SV) spanning from several years to thousands of years, and polar reversals occurring over millions of years (Mandea and Olsen, 2006). Owing to our incomplete understanding of the geodynamo and its dynamic process, we are currently unable to accurately predict trends in SV. Consequently, it is imperative to meticulously observe the spatiotemporal variations of geomagnetic fields to enhance our capabilities in positioning, navigation, and space plasma physics research.

There are two main data types used to study the SV of the geomagnetic field. One type of data is ground observatory data, which is used to study the sudden changes in SV, known as geomagnetic jerks. In recent years — specifically 2003, 2007, 2011, 2014, 2017, and 2021 — geomagnetic jerks have been identified using this method (Olsen and Mandea, 2008; Olsen et al., 2009; Chulliat and Maus, 2014; Torta et al., 2015; Khanyile and Nahayo, 2024). Some research has indicated that geomagnetic jerks originate from oscillatory phenomena in the outer core,

First author: J. Li, liojam@outlook.com
Correspondence to: B. Chen, champion_chb@126.com
Received 22 SEP 2024; Accepted 09 JAN 2025.
First Published online 24 FEB 2025.

which result in a regular period of jerks approximately every 3–4 years (Mandea et al., 2010; Chulliat and Maus, 2014). Several mathematical methods have also been employed to study jerks, including wavelet analysis, Slepian functions, and nonlinear analysis, with the aim of determining the time, duration, and distribution of jerks (Alexandrescu et al., 1996; Kim and von Frese, 2013; Qamili et al., 2013). Lately, Li YJ et al. (2023) conducted a study on the geomagnetic jerks from 2010 to 2021 and discovered global geomagnetic jerks in the eastward component *Y*. The occurrence time of the jerks within China and outside of China exhibited a 2-year lag, which may be attributed to the higher electrical conductivity of the deep mantle.

Another type of data is from the global spherical harmonic model of the geomagnetic field, used to study the spatiotemporal variation characteristics of SV. For example, CHAOS was established using data from LEO magnetic satellites and ground observatories, and describes the spatiotemporal distribution and variation characteristics of the geomagnetic field. Pavón-Carrasco et al. (2021) have researched the global distribution characteristics of the 2020 jerk, verifying its commencement time through an analysis of the global average secular acceleration (SA) pulse in the radial field during mid-2018. Campuzano et al. (2021) conducted a study to explore the relationship between the South Atlantic Anomaly (SAA) and global jerks, utilizing the CHAOS model. Their results indicate that over the past 20 years, the minimum value of the SAA's area extent change corresponds with the occurrence of jerks. Utilizing CHAOS 7-17, Bai CH et al. (2024) found that the appearance time of peak pulse at the Core Mantle Boundary (CMB) is consistent with that of jerks, which can be used as a new indicator for monitoring jerk occurrence. Both methods possess distinct advantages and disadvantages. Ground observatories are adept at monitoring the geomagnetic field, but their uneven spatial distribution presents challenges in studying global spatiotemporal variations. Also, while the geomagnetic field model can provide global information on SV and SA, its value at a specific location is derived from global data rather than localized data. This implies that it may be susceptible to noise from other locations (Hammer et al., 2022).

To address the aforementioned limitations, Mandea and Olsen (2006) proposed a new research method called Geomagnetic Virtual Observatory (GVO), which serves as a tool to extract the geomagnetic vector field time series at specific locations utilizing satellite measurements. Within the designated time window and localized area, the GVO method utilizes all available satellite data within the scope appropriate for scalar magnetic potential fitting, thereby calculating the geomagnetic field value at the target position. As shown in Figure 1, we typically designate the local area as a cylinder centered on a specific ground observatory. Given that the GVO relies solely on satellite data, it can extract the geomagnetic vector field time series at any location. In the first application of the GVO method by Mandea and Olsen (2006), they did not select satellite data based on any geomagnetic indices, nor consider changes in satellite orbit altitude. They only performed a second-order fitting for magnetic potential. Subsequent research has shown that signals from magnetospheric and ionospheric currents can influence the internal signal of GVO, and the monthly

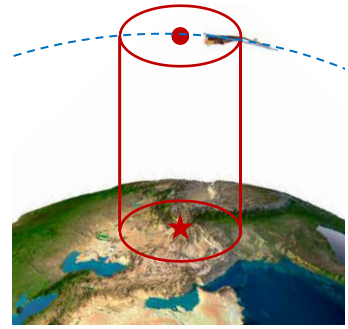

Figure 1. Illustration of the GVO method. The red point represents the Geomagnetic Virtual Observatory, the red pentagram represents a Ground Observatory (GOB), and the blue dashed line represents the satellite's orbit. The satellite geomagnetic measurements inside the cylinder are used to derive the geomagnetic field value at the target position (red point).

local time sampling bias of satellites could reduce the accuracy of the GVO method as well (Olsen and Mandea, 2007; Beggan et al., 2009; Shore, R. M., 2013; Domingos et al., 2019). Domingos et al. (2019), Cox et al. (2020), and Hammer et al. (2021) improved the GVO method by incorporating geomagnetic index criteria, elevating the order of magnetic potential fitting, and employing principal component analysis (PCA) to denoise GVO signals. The resulting GVO products have been instrumental in researching geomagnetic jerk (Hammer et al., 2022), outer core flow inversions (Kloss and Finlay, 2019; Rogers et al., 2019), and geodynamo data assimilation (Barrois et al., 2018; Huder et al., 2020).

The China Seismo-Electromagnetic Satellite (CSES) was launched on February 2, 2018; its orbit altitude is 507 km, and its inclination angle is 97.4° (Shen XH et al., 2018). CSES can provide high-precision measurements of the geomagnetic vector components and scalar values. Since its launch, CSES has shared a common operating period with Swarm. Together, these can be considered a 4-satellite combined constellation, significantly improving the spatiotemporal resolution of their measurements. In this paper, we first employed the GVO method to research geomagnetic SV in China and the surrounding area using CSES and Swarm datasets. We improve the setting of the virtual observatory's altitude and refine the extraction method for SV at the ground observatory based on the research of Hammer et al. (2021). Section 2 describes the data selection and preprocessing method for ground observatories and satellites. Section 3 introduces the details of the GVO and PCA methods. Section 4 presents the results of the core field and SV series, compared with the ground observatory and field model series. Finally, Section 5 concludes with a discussion of the GVO results and suggested improvements for the GVO method.

2. Data

2.1 Satellite Data

Considering the operating period of geomagnetic satellites and the accuracy of their measurements, we use data from the Swarm and CSES satellite missions to derive the GVO products. For the Swarm satellites, the data are obtained from the 1 Hz Level 1b product MAGX_LR_1B, version 0602/0603, encompassing all three satellites (Alpha, Bravo, and Charlie), collected between December 1, 2013 and December 31, 2023 (Beggan et al., 2013). For the CSES satellite, the data are obtained from the 1Hz Level 2 scientific HPM data, version 1.0, from January 1, 2019 to December 31, 2023 (Yang YY et al., 2021). Due to CSES orbit changes and other reasons, data on CSES from June 2021 to February 2022 is unavailable. Measurements are eliminated when satellite orbit adjustments and instrument malfunction occur.

Because the satellite passes through the same location at different local times each month, the satellite experiences different external magnetic field environments during different local times, resulting in a local time bias in the one-monthly products. Swarm satellites pass through the same sub-satellite point at the same local time approximately every four months. To balance the temporal resolution and reduce local time bias, we produce two types of GVO products on different time scales: one-monthly and four-monthly GVO series. For the raw 1 Hz geomagnetic field data, filtering methods can be classified according to two data chains: (1) for one-monthly series, and (2) for four-monthly series (Hammer et al., 2021). Figure 3 presents the flowchart of the satellite data preprocessing and model algorithm. Data chain (1) only uses a subsampling of 15 s to extract all available measurements. In contrast, data chain (2) also employs the sub-sampling interval of 15 s, and filters measurements based on specific criteria for dark and geomagnetic quiet periods:

(1) Model gross error: Calculate the difference between satellite measurements and CHAOS-7.18 model values, and remove measurements with a difference of more than 500 nT, model spherical harmonic degrees $n \in [1,13]$;

(2) Solar altitude angle: To minimize the ionospheric source interference as much as possible, only nighttime data are utilized, necessitating the sun to be positioned at least 10° below the horizon;

(3) Geomagnetic indices: To eliminate the effects of geomagnetic disturbances such as geomagnetic storms and sub storms, measurements during periods of strong geomagnetic activity are removed using geomagnetic indices (Olsen et al., 2014);

$$\begin{cases} Kp \le 2 \text{ and } \mathrm{d}|Kp|/\mathrm{d}t \le 2, \\ |Dst| \le 10 \text{ and } \mathrm{d}|Dst|/\mathrm{d}t \le 3. \end{cases} \tag{1}$$

Here, the unit of Dst is nT, and $\mathrm{d}|Dst|/\mathrm{d}t$ and $\mathrm{d}|Kp|/\mathrm{d}t$ respectively represent the variation values of Dst and Kp within 1 hour and 3 hours.

(4) Interplanetary Magnetic Field: Field-align current serves as the important pathway for the coupling of energy and mass between the magnetosphere and ionosphere, and it is also the main channel through which solar wind enters the magnetospheric–ionospheric system. In high latitude regions, the density structure of polar atmospheres can be influenced by mass and energy originating from interplanetary and solar sources, leading to complex ionospheric currents. The magnitude and direction of ionospheric currents at high latitudes are influenced by the interplanetary magnetic field (IMF) and merging electric field at the magnetopause E_m here $E_m = 0.33v^{4/3}B_t^{2/3}\sin^{8/3}(|\theta|/2)$. Using solar wind speed and IMF data, we filter satellite measurements based on the following conditions: $E_m \le 0.8$ mVm^{-1}; IMF $B_z > 0$ nT and $|B_y| < 10$ nT (Olsen et al., 2014; Friis-Christensen et al., 2017).

2.2 Ground Observatory Data

To validate the precision of GVO products, we choose 15 ground observatories from the International Real-time Magnetic Observatory Network (INTERMAGNET) and the Geomagnetic Network of China, Chinese Earthquake Administration. These observatories are almost evenly distributed throughout China and adjacent regions. Table 1 and Figure 2, respectively, show the latitude and longitude information and spatial distribution of these ground observatories. For observatories located outside of China, such as NVS, IRT, KHB, KAK, KNY, and GUA, we use the AUX_OBS datasets produced and distributed by the British Geological Survey (BGS), which have been checked and corrected for known baseline jumps based on the raw data from INTERMAGNET (Macmillan and Olsen, 2013). The Geomagnetic Network of China have checked the data from observatories within China and corrected baseline jumps. These data comprise hourly average values of the geomagnetic field components X, Y, and Z, covering the period from 2014 to 2023. We further select three "benchmark" observa-

Table 1. Latitude and longitude of the ground observatories.

IAGA code	Latitude	Longitude
NVS	54.9°	83.2°
IRT	52.2°	104.5°
MZL	49.6°	117.4°
KHB	47.6°	134.7°
WMQ	44.4°	86.9°
JYG	39.8°	98.2°
CHL	39.7°	119.0°
KSH	39.5°	76.0°
KAK	36.2°	140.2°
LZH	36.1°	103.9°
KNY	31.4°	130.9°
CDP	31.0°	103.7°
QZH	24.9°	118.6°
GZH	22.9°	112.5°
GUA	13.6°	144.9°

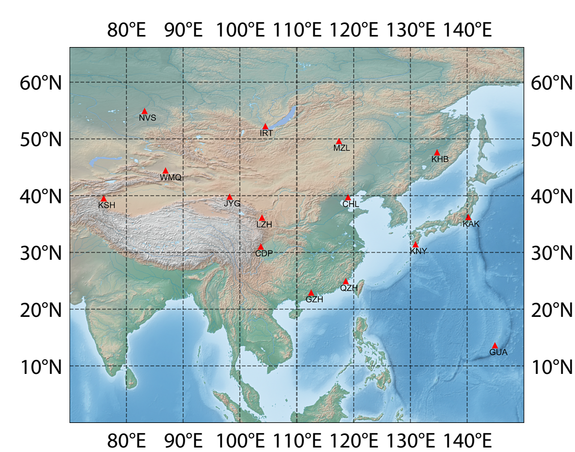

Figure 2. Distribution of the ground observatories.

tories (IRT, KAK, WMQ) from these observatories to validate the consistency between GVO products and the series of ground observatories, especially the accuracy in capturing the SV trend.

The measurements from the ground observatories are collected from a combination of multiple internal and external field sources. When researching the internal geomagnetic field, external sources are typically regarded as noises. External noises include the electric currents of the ionosphere and magnetosphere, as well as their interactions with the solar wind. Therefore, it is necessary to process the hourly mean values from the ground observatory to extract the core field and SV series. The specific methods are as follows:

(1) External field model: Remove values of the CHAOS magnetospheric field and ionospheric field, including their induced counterparts, from the hourly mean values (Sabaka et al., 2018; Finlay et al., 2020);

(2) Solar altitude angle: The sun to be positioned at least 10° below the horizon;

(3) Geomagnetic indices:

$$\begin{cases} Kp \le 2 \text{ and } \mathrm{d}|Kp|/\mathrm{d}t \le 2, \\ |Dst| \le 10 \text{ and } \mathrm{d}|Dst|/\mathrm{d}t \le 3. \end{cases} \tag{2}$$

Here, the unit of *Dst* is nT, and d|*Dst*|/d*t* and d|*Kp*|/d*t* respectively represent the variation values of *Dst* and *Kp* within 1 hour and 3 hours.

(4) International geomagnetic quiet days: We choose the international 5 quietest days each month using the international Q-days data from the World Data Center for Geomagnetism (WDC). Subsequently, we calculate the monthly mean values from the hourly mean values that have been filtered through the aforementioned steps;

3. Method

3.1 Extracting SV Time-Series

The SV is one of the main characteristics of the core field, mainly manifested in slow changes on a hundred- to thousand-year scale,

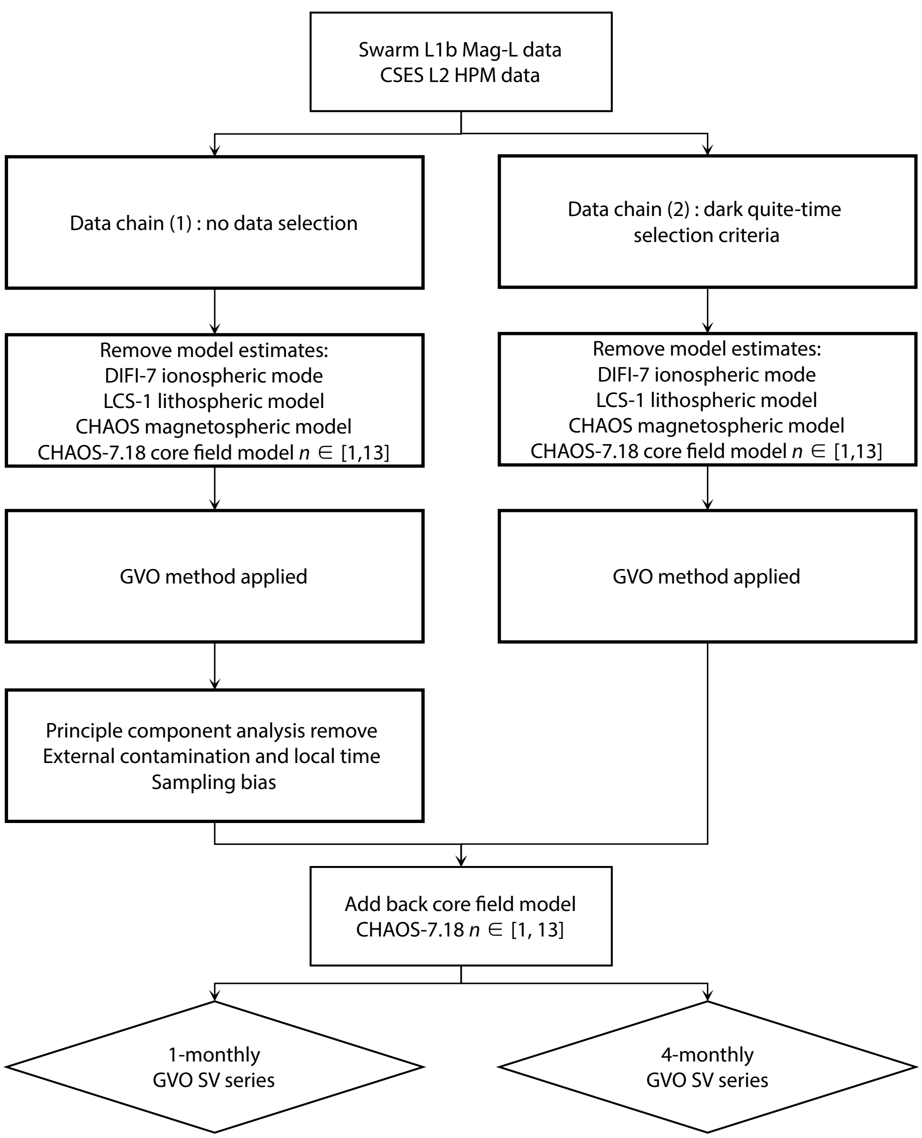

Figure 3. Overview of the process from satellite measurements to GVO products.

and considered linearly changing in the short term of 1−2 years. The SV of each element of the geomagnetic field can be directly observed through the annual mean series obtained from the geomagnetic observatory. Extracting the SV series from the core field series is equivalent to extracting the annual variation rate series of the core field. The method employed for extracting the SV series is the same for both the GVO and GOB series. We extract SV by calculating the annual difference of monthly means (ADMM):

$$\frac{\partial \boldsymbol{B}}{\partial t}(t_{n-6}) = \boldsymbol{B}(t_n) - \boldsymbol{B}(t_{n-12}), \tag{3}$$

where $\boldsymbol{B}$ is the geomagnetic component, and t is the month. ADMM reduces noises and eliminates annual variations; it can extract SV without introducing the smoothing effect that results from methods involving longer period averages (Brown et al., 2013; Cox et al., 2018).

3.2 Overview of Virtual Observatory

We define a cylinder with a ground observatory at the center of its lower surface and a virtual observatory on its upper surface, called the GVO cylinder. It is necessary to determine the height h_{GVO} and radius r_d of the cylinder and extract satellite measurements within the cylinder that also meet the relevant data filtering chains. For setting specific values of h_{GVO}, the height of GVO cylinder, Hammer et al. (2021) set h_{GVO} = 490 km, corresponding to the average orbital height of the Swarm satellites from 2013 to 2020. However, a limitation of this approach is that it ignores the gradual decrease in orbital height during the satellite operating period. Considering this, we set the different h_{GVO} for each time window (one or four months), and the value set as the average orbital height of all satellites during each time window. For setting specific values of r_d, the radius of the GVO cylinder, considering the relationship between the r_d and the spherical harmonic order n is $r_d \sim \pi(r_a + h_{\mathrm{GVO}})/\sqrt{n(n+1)}$, here r_a = 6371.2 km is Earth's average radius, n is spherical harmonic order (Backus et al., 1996). We need to ensure sufficient measurements within the cylinder to obtain robust GVO estimation while ensuring high spatial resolution of GVO. In this research, we set the r_d to 700 km, equivalent to spherical harmonic order $n = 14$.

For one-monthly GVO products, the time point corresponding to each GVO data is the 15$^{\mathrm{th}}$ day of each month. For four-monthly GVO products, as they are calculated on measurements from January to April, May to August, and September to December, the corresponding time point for each GVO data is the first day of the third month within these four-month intervals. By calculating the annual difference of one-monthly and four-monthly GVO products, we can obtain the GVO SV products corresponding to the time interval. This causes the time point corresponding to GVO SV products to be advanced by 6 months compared to the GVO products.

3.3 Data Pre-Processing

Before using satellite measurements for GVO estimation, the first step is pre-whitening the data. Data pre-whitening is a preprocessing method utilized in signal processing and series analysis, aimed at removing auto-correlation from data and making it closer to white noise. White noise, characterized by equal power at all frequencies and no correlation, is a random signal without regularity or periodicity (Hammer et al., 2021). In this study, we achieve pre-whitening by extracting residuals between satellite measurements and the model, which are used to derive the robust GVO estimation. For the vector geomagnetic field measured by satellite $\boldsymbol{B}_{\mathrm{obs}}$, the following equation calculates its residual with the model:

$$\delta B^j_{\mathrm{core}} = B^j_{\mathrm{obs}} - B^j_{\mathrm{MF}} - B^j_{\mathrm{lith}} - B^j_{\mathrm{mag}} - B^j_{\mathrm{iono}}. \tag{4}$$

Here j represents components in different directions, $j = r$, θ, or φ ; B_{MF} is the core field, calculated by the CHAOS-7.18, SH degrees $n \in [1,13]$; B_{lith} is the lithospheric field, calculated by the LCS-1, SH degrees $n \in [14,185]$; B_{mag} is the magnetospheric field and its induced field, also calculated by the CHAOS-7.18 model; B_{iono} is the ionospheric field and its induced field, calculated by the DIFI-7 model (Olsen et al., 2017; Sabaka et al., 2018; Finlay et al., 2020; Hammer et al., 2021). Hammer (2018) analyzed GVO products derived with and without the pre-whitening process. The results indicated that GVO products, when not utilizing pre-whitening data, are more susceptible to interference from abnormal measurements and display larger errors when compared to ground observatory data.

Previous researches have demonstrated that using along-track differences of the satellite measurements when establishing a geomagnetic field model can improve the field's spatial resolution (Kotsiaros et al., 2015). The differences effectively remove external noises, especially degree-1 external fields caused by varying magnetospheric ring currents (Olsen et al., 2015; Kotsiaros, 2016). Data along-track sums must also be considered to obtain comprehensive information on the longer wavelengths of the core field (Sabaka et al., 2013).

For satellite vector geomagnetic field residual at a certain position $\boldsymbol{r}$, $\delta B_j(\boldsymbol{r})$, here j represents components in different directions, $j = r$, θ, or φ. $\sum d_j$ and Δd_j mean sums and differences of the vector geomagnetic field components. Considering that Swarm Alpha and Charlie are flying side by side on a parallel course, it is feasible to calculate the differences and sums along their tracks (AT), and those in the east-west direction (EW). The final differences and sums used for the GVO method is the combination of AT and EW, such as $\sum d_j = (\sum d_j^{\mathrm{AT}}, \sum d_j^{\mathrm{EW}})$ and $\Delta d_j = (\Delta d_j^{\mathrm{AT}}, \Delta d_j^{\mathrm{EW}})$. Sums and differences are calculated as:

$$\begin{cases} \sum d_j^{\mathrm{AT}} = [\delta B_j(\boldsymbol{r},t) + \delta B_j(\boldsymbol{r} + \Delta \boldsymbol{r}, t+15)]/2, \\ \Delta d_j^{\mathrm{AT}} = [\delta B_j(\boldsymbol{r},t) - \delta B_j(\boldsymbol{r} + \Delta \boldsymbol{r}, t+15)], \end{cases} \tag{5}$$

$$\begin{cases} \sum d_j^{\mathrm{EW}} = [\delta B_j^{\mathrm{Alpha}}(\boldsymbol{r}_a, t_a) + \delta B_j^{\mathrm{Charlie}}(\boldsymbol{r}_c, t_c)]/2, \\ \Delta d_j^{\mathrm{EW}} = [\delta B_j^{\mathrm{Alpha}}(\boldsymbol{r}_a, t_a) - \delta B_j^{\mathrm{Charlie}}(\boldsymbol{r}_c, t_c)]. \end{cases} \tag{6}$$

For Δd_j^{AT} and $\sum d_j^{\mathrm{AT}}$, the satellite's speed is approximately 7.7 km/ s, and a 15 s AT difference is equivalent to 115 km in space (Olsen et al., 2015). For Δd_i^{EW} and $\sum d_i^{\mathrm{EW}}$, the east–west orbit separation between Alpha and Charlie is approximately 1.4°, corresponding to 155 km (Olsen et al., 2015). In addition, to ensure that Alpha and Charlie are be closest in latitude, we require that $|\Delta t| = |t_a - t_c| < 50$ s.

3.4 Geomagnetic Virtual Observatory Method

In the original satellite data file, the satellite vector measurements are given as B_r, B_θ, B_φ in accordance with the Earth-Centered-Earth-Fixed (ECEF) coordinate system. Before deriving the GVO estimation, it is necessary to transform the position of the residual field in the ECEF coordinate system to a local Cartesian coordinate system, centered on each virtual observatory. Figure 4 shows a sketch map of two coordinate systems, the coordinate transformation process can be divided into two distinct, sequential steps:

(1) The residual vector field and its position, as well as the position of the virtual observatory, first need to be transformed from the spherical polar coordinate to a Cartesian coordinate within the ECEF coordinate system. The transformation relationship from $(r,\theta,\varphi)_{\mathrm{ECEF}}$ to $(x,y,z)_{\mathrm{ECEF}}$ is as follows:

$$\begin{bmatrix} x \\ y \\ z \end{bmatrix}_{\mathrm{ECEF}} = r\begin{bmatrix} \sin\theta\cos\varphi \\ \sin\theta\sin\varphi \\ \cos\theta \end{bmatrix}_{\mathrm{ECEF}}. \tag{7}$$

Here $r \geq 0$, $0 \leq \theta \leq \pi$ and $0 \leq \varphi \leq 2\pi$.

(2) The residual vector field and its position are then transformed from the ECEF coordinate system to the local Cartesian right-hand coordinate system. In this coordinate local system, the x-axis points south, the y-axis points east, and the z-axis points vertically upward. It is also known as the SEU (South, East, Up) coordinate system. The transformation relationship from $(x,y,z)_{\mathrm{ECEF}}$ to $(x,y,z)_{\mathrm{SEU}}$ is as follows:

$$\begin{bmatrix} x \\ y \\ z \end{bmatrix}_{\mathrm{SEU}} = \begin{bmatrix} \cos\theta\cos\varphi & \cos\theta\sin\varphi & -\sin\varphi \\ -\sin\varphi & \cos\varphi & 0 \\ \sin\theta\sin\varphi & \sin\theta\sin\varphi & \cos\theta \end{bmatrix}\begin{bmatrix} x \\ y \\ z \end{bmatrix}_{\mathrm{ECEF}}. \tag{8}$$

(3) The height of the virtual observatory h_{GVO} need to be subtracted from the z-coordinate, which moves the origin of the local coordinate system from GOB to GVO.

We usually assume that satellite measurements are measured in source-free regions. Therefore, the geomagnetic scalar potential V associated with the residual geomagnetic field, $\delta\boldsymbol{B}$, satisfies Laplace's equation $\nabla^2 V = 0$, and the potential is related to the residual field by $\delta\boldsymbol{B} = -\nabla V$ (Hammer et al., 2021). The solution of Laplace's equation can be expressed as the sum of harmonic polynomials (Backus et al., 1996):

$$V(x,y,z) = \sum_{l=1}^{L} R_{abc}x^a y^b z^c = R_{000}+R_{100}x+R_{010}y+R_{001}z+R_{200}x^2+R_{020}y^2 + R_{002}z^2+R_{110}xy+R_{101}xz+R_{011}yz+R_{300}x^3+R_{030}y^3+R_{003}z^3+R_{210}x^2y + R_{201}x^2z+R_{120}y^2x+R_{021}y^2z+R_{102}z^2x+R_{012}z^2y+R_{111}xyz+\cdots. \tag{9}$$

Here, x, y, and z are spatial coordinates in the local coordinate system; $l = a + b + c$; a, b, and c are non-negative integers; the L represents the expansion order; R_{abc} is the polynomial coefficient. For a GVO cylinder radius of 700 km, we consider the orbit height variation of the satellites and decide to expand the harmonic polynomials to cubic order, i.e. $L = 3$. This equation has 20 parameters in the above expansion.

As is well known, the geomagnetic field is a solenoidal irrotational vector field. It satisfies two conditions: (1) $\nabla\times\delta\boldsymbol{B} = 0$ ($\nabla\times\nabla V = 0$); (2) $\nabla\cdot\delta\boldsymbol{B} = 0$ ($\nabla\cdot\nabla V = 0$). By applying the above two conditions, we simplify the geomagnetic potential harmonic polynomials. The final expansion decreases the number of parameters to 15.

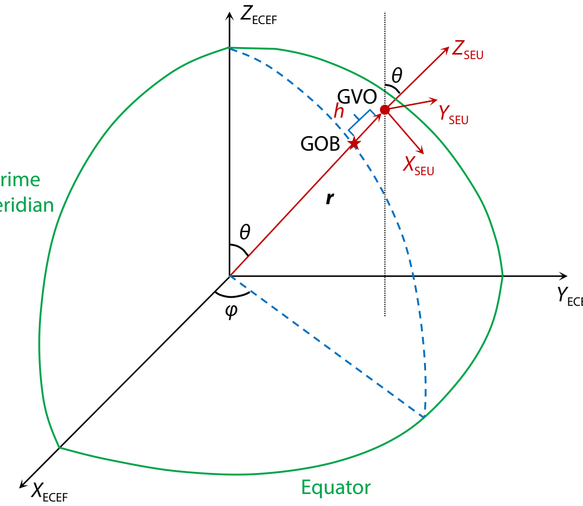

Figure 4. Sketch map of ECEF and SEU coordinate system with virtual observatory as the origin.

$$V(x,y,z) = R_{100}x+R_{010}y+R_{001}z+R_{200}x^2+R_{020}y^2-(R_{200}+R_{020})z^2+2R_{110}xy + 2R_{101}xz+2R_{011}yz-(R_{102}+R_{120})x^3-(R_{210}+R_{012})y^3-(R_{201}+R_{021})z^3 + 3R_{210}x^2y+3R_{201}x^2z+3R_{120}y^2x+3R_{021}y^2z+3R_{102}z^2x + 3R_{012}z^2y+6R_{111}xyz. \tag{10}$$

An observation equation can be formulated based on the relationship between the geomagnetic vector field and geomagnetic potential.

$$\begin{cases} X = -B_\theta = \dfrac{\partial V}{\partial x}, \\ Y = B_\varphi = -\dfrac{\partial V}{\partial y}, \\ Z = -B_r = \dfrac{\partial V}{\partial z}. \end{cases} \tag{11}$$

After establishing the observation equation, we derive a linear forward problem for the matrix $\boldsymbol{m}$, consisting of the expansion coefficients R_{abc}, and the matrix $\boldsymbol{d}$ consisting of the residual geomagnetic field components (δB_x, δB_y, δB_z) in SEU.

$$\boldsymbol{d} = \boldsymbol{G}\boldsymbol{m}. \tag{12}$$

Here, $\boldsymbol{G}$ is the matrix composed of spatial derivatives of geomagnetic potential. For the vector data, the specific description of the Equation (10) is as follows:

$$\boldsymbol{d} = \begin{bmatrix} \delta B_x(r_1) \\ \vdots \\ \delta B_x(r_n) \\ \delta B_y(r_1) \\ \vdots \\ \delta B_y(r_n) \\ \delta B_z(r_1) \\ \vdots \\ \delta B_z(r_n) \end{bmatrix}, \tag{13}$$

$$\boldsymbol{G}=\begin{bmatrix} -1 & 0 & 0 & -2x_1 & 0 & -2y_1 & -2z_1 & 0 & -6x_1y_1 & \cdots \\ \vdots & \vdots & \vdots & \vdots & \vdots & \vdots & \vdots & \vdots & \vdots & \cdots \\ -1 & 0 & 0 & -2x_n & 0 & -2y_n & -2z_n & 0 & -6x_ny_n & \cdots \\ 0 & -1 & 0 & 0 & -2y_1 & -2x_1 & 0 & -2z_1 & -3x_1^2-3y_1^2 & \cdots \\ \vdots & \vdots & \vdots & \vdots & \vdots & \vdots & \vdots & \vdots & \vdots & \cdots \\ 0 & -1 & 0 & 0 & -2y_n & -2x_n & 0 & -2z_n & -3x_n^2-3y_n^2 & \cdots \\ 0 & 0 & -1 & 2z_1 & 2z_1 & 0 & -2x_1 & -2y_1 & 0 & \cdots \\ \vdots & \vdots & \vdots & \vdots & \vdots & \vdots & \vdots & \vdots & \vdots & \cdots \\ 0 & 0 & -1 & 2z_n & 2z_n & 0 & -2x_n & -2y_n & 0 & \cdots \end{bmatrix}$$
$$\begin{bmatrix} -6x_1z_1 & -3y_1^2-3z_1^2 & -3z_1^2-3x_1^2 & 0 & 0 & 0 \\ \vdots & \vdots & \vdots & \vdots & \vdots & \vdots \\ -6x_nz_n & -3y_n^2-3z_n^2 & -3z_n^2-3x_n^2 & 0 & 0 & 0 \\ 0 & -6x_1y_1 & 0 & -6y_1z_1 & -3z_1^2-3y_1^2 & 0 \\ \vdots & \vdots & \vdots & \vdots & \vdots & \vdots \\ 0 & -6x_ny_n & 0 & -6y_nz_n & -3z_n^2-3y_n^2 & 0 \\ -3z_1^2-3x_1^2 & 0 & -6x_1z_1 & -3z_1^2-3y_1^2 & -6y_1z_1 & 0 \\ \vdots & \vdots & \vdots & \vdots & \vdots & \vdots \\ -3z_n^2-3x_n^2 & 0 & -6x_nz_n & -3z_n^2-3y_n^2 & -6y_nz_n & 0 \end{bmatrix}, \tag{14}$$

$$\boldsymbol{m}=\begin{bmatrix} R_{100} \\ R_{010} \\ R_{001} \\ R_{200} \\ R_{020} \\ R_{110} \\ R_{101} \\ R_{011} \\ R_{210} \\ R_{201} \\ R_{120} \\ R_{102} \\ R_{021} \\ R_{012} \\ R_{111} \end{bmatrix}. \tag{15}$$

Considering the sums and differences of the residual geomagnetic field for along-track and east-west direction, we expand the matrices $\boldsymbol{d}$ and $\boldsymbol{m}$ employed for GVO estimation. The designed matrices using sums and differences are as $\boldsymbol{d}=\Delta d_x; \Delta d_y; \Delta d_z; \sum d_x; \sum d_y; \sum d_z$, $\boldsymbol{G}=\Delta G_x; \Delta G_y; \Delta G_z; \sum G_x; \sum G_y; \sum G_z$, here $\Delta G_i = G_i(r_1)-G_i(r_2)$ and $\sum G_i = [G_i(r_1)+G_i(r_2)]/2$, $i=(x, y, z)$.

Based on the designed matrices of $\boldsymbol{d}$ and $\boldsymbol{G}$, we use the weighted least-squares inversion method to estimate the expansion coefficients of the GVO model:

$$\boldsymbol{m}=(\boldsymbol{G}^{\mathrm{T}}\boldsymbol{WG})^{-1}\boldsymbol{GWd}. \tag{16}$$

Here, $\boldsymbol{W}$ is a diagonal weight matrix, consisting of Huber weights for each data vector in the matrix $\boldsymbol{m}$. Considering that Swarm Alpha and Charlie fly side-by-side and yield analogous measurements, a down-weight factor of 1/2 is assigned to the data obtained from these satellites.

After determining the geomagnetic potential equation in the local Cartesian coordinate, the estimation of residual geomagnetic field components at the virtual observatory ($x=0$, $y=0$, $z=0$) is calculated as:

$$\delta\boldsymbol{B}_{\mathrm{GVO}}=-\nabla V(0,0,0)=-\begin{pmatrix} R_{100} \\ R_{010} \\ R_{001} \end{pmatrix}. \tag{17}$$

In the last step, we need to add back the value of the core field model $\boldsymbol{B}_{\mathrm{GVO}}^{\mathrm{MF}}(\boldsymbol{r},t)$, for each GVO position and its time point. We use the CHAOS-7.18 model for SH degrees $n\in[1,13]$. Finally we derive the GVO series.

$$\boldsymbol{B}_{\mathrm{GVO}}(\boldsymbol{r},t)=\delta\boldsymbol{B}_{\mathrm{GVO}}(\boldsymbol{r},t)+\boldsymbol{B}_{\mathrm{GVO}}^{\mathrm{MF}}(\boldsymbol{r},t). \tag{18}$$

3.5 Principal Components Analysis

The one-monthly GVO products have two primary sources of noise: (1) external source signals contained in the measurements, because we do not select the satellite measurements, nor remove values of the magnetosphere and ionosphere; (2) local time sampling bias affecting the GVO estimation. To resolve these issues, we apply the principal component analysis (PCA) method described by Cox et al. (2018) to isolate and eliminate the external signals from the one-monthly GVO products.

Domingos et al. (2019) applied PCA on the GVO series, and their findings revealed the model associated with the large-scale internal field, as well as the special model linked to annual variations in the external field. We employ the PCA on the SV residuals to derive proxy signals for external signals and remove them from the original SV residuals. The GVO SV series are calculated by using ADMM, and the SV residuals are the differences between the GVO SV series and the SV series calculated by CHAOS-7.18 at the same times and positions, SH degrees $n\in[1,13]$ (Hammer et al., 2021). The coherent signal between the SV residual of the X, Y, and Z components for a virtual observatory can be described by a 3×3 covariance matrix:

$$\mathrm{cov}(\boldsymbol{P},\boldsymbol{Q})=\frac{\sum_{i=1}^{n}\boldsymbol{P}_i\boldsymbol{Q}_i}{n}. \tag{19}$$

Here, $\boldsymbol{P}$ and $\boldsymbol{Q}$ are vectors of SV residuals, and n is the length of the vector. For a single GVO observatory, we calculate eigenvalues and eigenvectors of the covariance matrix. Different eigenvalues denote distinct degrees of contribution of eigenvectors to the external field. When considering N GVO observatories, the dimension of the SV residual covariance matrix is $3N \times 3N$, and it can be decomposed into up to $3N$ eigenvalues and their corresponding eigenvectors. The projection of SV residual on K dominant eigenvectors serves as the proxy signal for the external field. In these feature directions, we remove the proxy signal from the residual matrix based on the contribution of each component to the external field proxy signal (Cox et al., 2018):

$$\dot{\boldsymbol{R}}_i = \boldsymbol{R}_i - \frac{\sum_{j=1}^{K} \boldsymbol{R}_i \boldsymbol{P}_j}{\sum_{j=1}^{K} (\boldsymbol{P}_j)^2} \boldsymbol{P}_j. \tag{20}$$

Here, $\boldsymbol{R}$ is the original residual matrix; $\dot{\boldsymbol{R}}$ is the denoising residual matrix; $\boldsymbol{P}$ is the external field proxy signal; and i is the number of rows in the residuals matrix, $i = 1, 2, \ldots, 3N$; j is number of the eigenvectors, $j = 1, 2, \ldots, K$.

Cleaner internal signals could be obtained by removing more projections on eigenvectors. However, it is essential to verify that the residuals in these directions correspond to external field signals. Otherwise, information related to the internal field may also be inadvertently removed. The value of K depends on how many Principal Components (PCs) can be identified as the external field signals. Cox et al. (2020) analyzed temporal variations of the external proxy signal with Disturbance Storm Time (*Dst*) index, ap index, and auroral electrojet (*AE*) index. They further compared the discrete Fourier transforms of these signals to ascertain if the proxy signal represents an external field signal. Due to the variations in external noise sources of observatories at different locations, Cox et al. (2020) divided observatories into five regions based on their geomagnetic latitude, each with a different number of PCs. Table 2 from Cox et al. (2020) shows the number of PCs identified as external noise, and the cumulative percentage variance of these PCs within each designated region.

In the final step, we numerically integrate the denoised GVO SV series to generate one-monthly GVO core field series.

Table 2. The number and total percentage variance of PCs in each region (Cox et al., 2020).

Region	Magnetic latitude, λ_m	Number of PCs	Total percentage of variance
Polar North	$70° \le \lambda_m \le 90°$	4	85.1%
Auroral North	$50° \le \lambda_m \le 70°$	3	83.3%
Low-mid Lats	$-50° \le \lambda_m \le 50°$	4	88.6%
Auroral South	$-70° \le \lambda_m \le -50°$	3	79.3%
Polar South	$-90° \le \lambda_m \le -70°$	4	82.8%

4. Results

4.1 Validation with Ground Observatory and Field Model

Through the above steps, we obtain the four types of data: one-monthly GOB core field series, four-monthly GOB core field series, one-monthly GVO core field series, and four-monthly GVO core field series. To facilitate direct comparisons with the ground observatories series, we extend the GVO series to the ground by subtracting the field difference between the ground observatory and the GVO altitudes determined by the core field model, and the local crustal bias. We then Calculate the ADMM of the core field series and obtain the SV series. To quantitatively analyze the GVO products' quality, we calculate their root mean square error (RMSE) with the ground observatories series and CHAOS-7.18 model as:

$$\text{RMSE}^j_{\text{obs}} = \sqrt{\frac{1}{N}\sum_{i=1}^{N}[B^j_{\text{GVO}}(t_i) - B^j_{\text{GOB}}(t_i)]^2}, \tag{21}$$

$$\text{RMSE}^j_{\text{Mod}} = \sqrt{\frac{1}{N}\sum_{i=1}^{N}[B^j_{\text{GVO}}(t_i) - B^j_{\text{Mod}}(t_i)]^2}. \tag{22}$$

Here $\boldsymbol{B}_{\text{GVO}}$ is GVO series, $\boldsymbol{B}_{\text{GOB}}$ is ground observatories series, $\boldsymbol{B}_{\text{Mod}}$ is field model series, $i = 1, 2, \cdots, N$, N is the number of data, j represents a spherical polar component r, θ, and φ. The model series are calculated using the CHAOS-7.18 model SH degrees $n \in [1, 13]$. For the RMSE of the SV series, just replace the core field series in the formula (21) and (22) with the SV series.

4.1.1 *Accuracy of GVO series in core field*

To illustrate the results of the GVO core field series, Table 3 shows the validation results with the ground observatories and geomagnetic core field model for the one-monthly GVO series. Table 4 shows similar results for the four-monthly GVO series. Figures 5 and 6 show one-monthly and four-monthly core field series. Due to space constraints, we show the series from eight ground observatories with uniform spatial distribution. The GVO series obtained by using only Swarm data, only CSES data, and both data types are shown in the figures. For the GVO (Swarm+CSES) series, during the period without CSES data, their values are the same as GVO (Swarm) values, and completely overlap in the figures. The red shaded areas in the figures represent the periods of high solar activity, defined by the SILSO (Sunspot Index and Long-term Solar Observations) provided by the Royal Observatory of Belgium.

We calculated the RMSE between the core field series; Tables 3 and 4 contain the relevant results, showing that the GVO series align well with the GOB and CHAOS series. Most RMSE values for the one-monthly and four-monthly GVO series are less than 5 nT and 3 nT compared to the GOB series. The INTERMAGNET standard for the quasi-definitive data requires an RMSE of less than 5 nT. This standard suggests that the GVO series can replace the GOB series, particularly the four-monthly GVO series. The mean RMSE of the benchmark observatories represents the highest accuracy achievable by the GVO method. In the r, θ, and φ component of the geomagnetic field, the accuracies are 2.71 nT, 2.32 nT, and 2.24 nT.

By calculating the RMSE between the GVO, CHAOS, and GOB series, we can obtain the GVO method's accuracy relative to the CHAOS model. From Tables 3 and 4, we can obtain that for the one-monthly series, both in the r and θ components. The highest accuracy of the GVO are respectively 48% and 24% higher than

Table 3. Summary of comparisons for the one-monthly core field series.

	One-monthly core field series (nT)								
	GVO vs GOB			CHAOS vs GOB			GVO vs CHAOS		
	$RMSE_r$	$RMSE_\theta$	$RMSE_\varphi$	$RMSE_r$	$RMSE_\theta$	$RMSE_\varphi$	$RMSE_r$	$RMSE_\theta$	$RMSE_\varphi$
NVS	3.24	2.97	1.80	5.98	5.25	1.92	2.68	2.63	1.76
IRT	2.79	2.41	2.35	5.19	4.17	2.91	2.48	2.15	2.28
MZL	3.06	2.66	3.54	2.97	4.53	3.37	2.78	2.24	3.37
KHB	3.07	2.70	3.21	2.17	1.41	2.93	2.72	2.44	1.93
WMQ	3.69	3.79	2.47	10.2	5.18	2.50	3.21	3.32	2.38
JYG	6.73	5.66	3.04	12.4	4.50	2.35	5.07	3.87	2.35
CHL	4.64	4.16	5.13	2.04	3.18	5.98	2.04	3.69	3.98
KSH	7.68	5.94	4.46	9.20	5.20	3.14	4.42	4.10	3.14
KAK	2.55	2.54	2.34	1.76	2.08	2.11	2.19	2.21	1.11
LZH	5.51	5.87	3.99	13.9	6.37	2.79	4.67	3.64	2.79
KNY	3.84	2.53	1.78	2.32	1.99	1.98	2.32	2.18	0.98
CDP	4.61	6.91	5.51	9.29	6.35	4.53	3.59	3.57	3.53
QZH	1.71	4.50	2.57	1.80	3.08	1.76	1.56	3.97	1.76
GZH	1.51	2.96	2.20	1.87	2.55	1.41	1.27	2.68	1.41
GUA	2.44	3.98	4.57	3.25	3.54	3.76	2.45	3.27	1.96
Mean	3.81	3.97	3.26	5.63	3.96	2.90	2.90	3.22	2.30
B-mean	3.01	2.91	2.39	5.75	3.81	1.84	2.63	2.56	1.92

Note：B-mean: the mean value of Benchmark observatories.

Table 4. Summary of comparisons for the four-monthly core field series.

	Four-monthly core field series (nT)								
	GVO vs GOB			CHAOS vs GOB			GVO vs CHAOS		
	$RMSE_r$	$RMSE_\theta$	$RMSE_\varphi$	$RMSE_r$	$RMSE_\theta$	$RMSE_\varphi$	$RMSE_r$	$RMSE_\theta$	$RMSE_\varphi$
NVS	3.04	2.69	1.78	4.33	2.69	1.85	2.42	2.24	0.85
IRT	2.58	1.47	2.35	5.07	2.84	2.34	2.12	1.94	1.54
MZL	2.19	2.36	3.24	1.87	2.48	4.37	1.68	2.23	3.19
KHB	1.83	1.62	2.50	2.61	1.85	1.79	1.55	2.02	1.79
WMQ	3.91	3.22	2.38	10.2	3.41	1.91	2.87	2.59	0.91
JYG	6.26	3.48	2.21	9.36	4.07	1.90	3.69	3.32	0.90
CHL	2.19	2.37	4.38	1.00	2.24	4.33	1.00	2.97	3.32
KSH	3.60	3.93	3.47	9.76	3.66	3.59	2.50	3.66	2.24
KAK	1.64	2.28	2.00	1.46	1.37	2.02	1.46	1.86	1.02
LZH	4.41	4.04	3.69	8.81	3.87	2.65	2.84	2.56	2.65
KNY	1.79	2.27	2.64	1.23	2.22	2.47	1.23	1.22	1.47
CDP	2.56	2.76	2.63	12.5	2.07	2.74	2.44	2.49	1.41
QZH	3.14	2.76	2.77	1.67	2.32	2.82	1.67	1.22	1.82
GZH	2.12	3.72	3.27	2.42	2.87	2.37	1.92	1.77	1.37
GUA	2.19	2.44	1.85	3.22	2.52	2.24	2.02	2.52	1.24
Mean	2.90	2.76	2.75	5.04	2.70	2.63	2.09	2.31	1.72
B-mean	2.71	2.32	2.24	5.59	2.54	2.09	2.15	2.13	1.16

Note：B-mean: the mean value of Benchmark observatories.

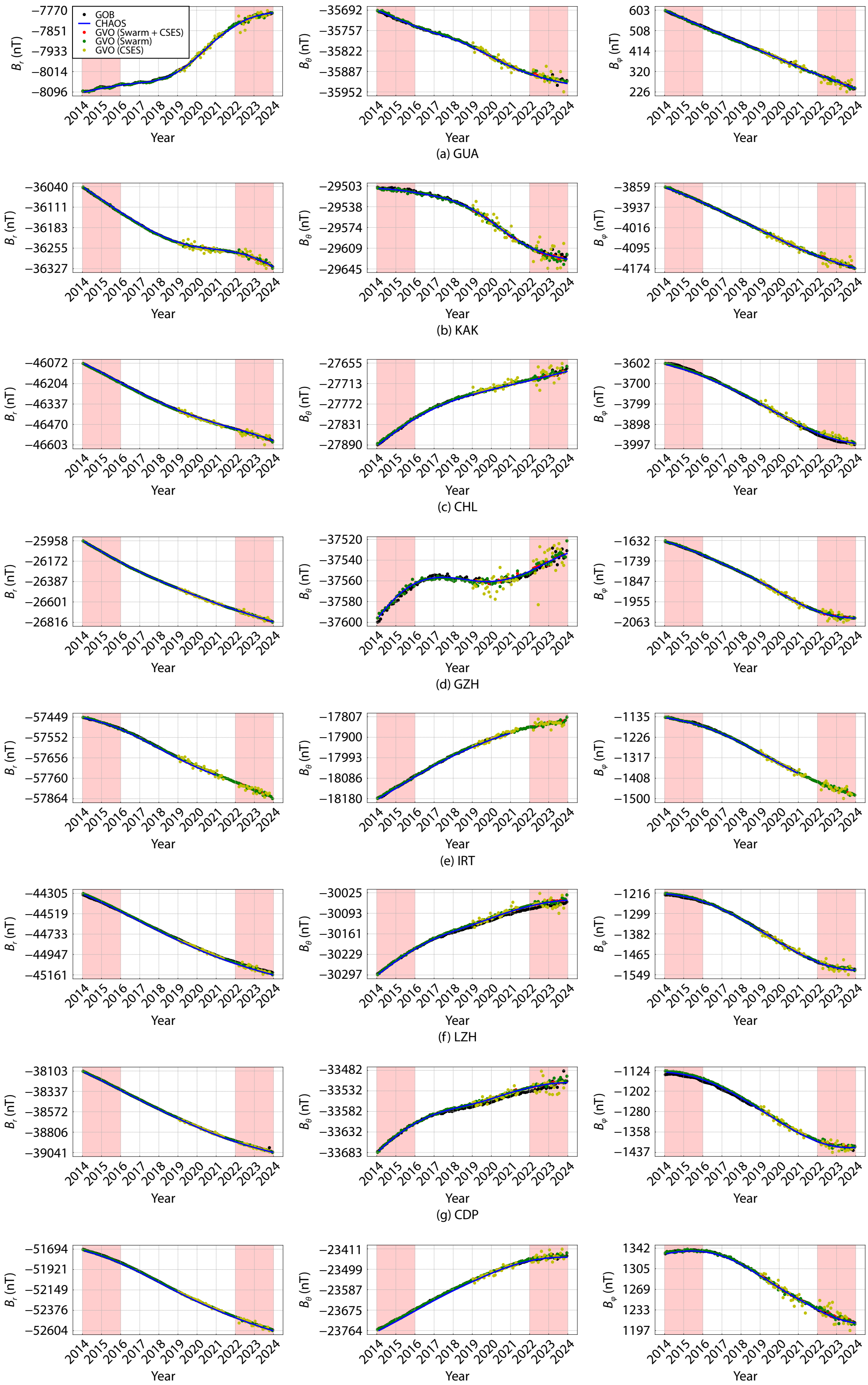

Figure 5. One-monthly core field series: black dots are the GOB series, red dots are the GVO (Swarm+CSES) series, green dots are the GVO (Swarm) series, yellow dots are the GVO (CSES) series, blue line is the CHAOS series, red shaded areas represent the period of high solar activity. Each column from left to right is the B_r, B_θ and B_φ component.

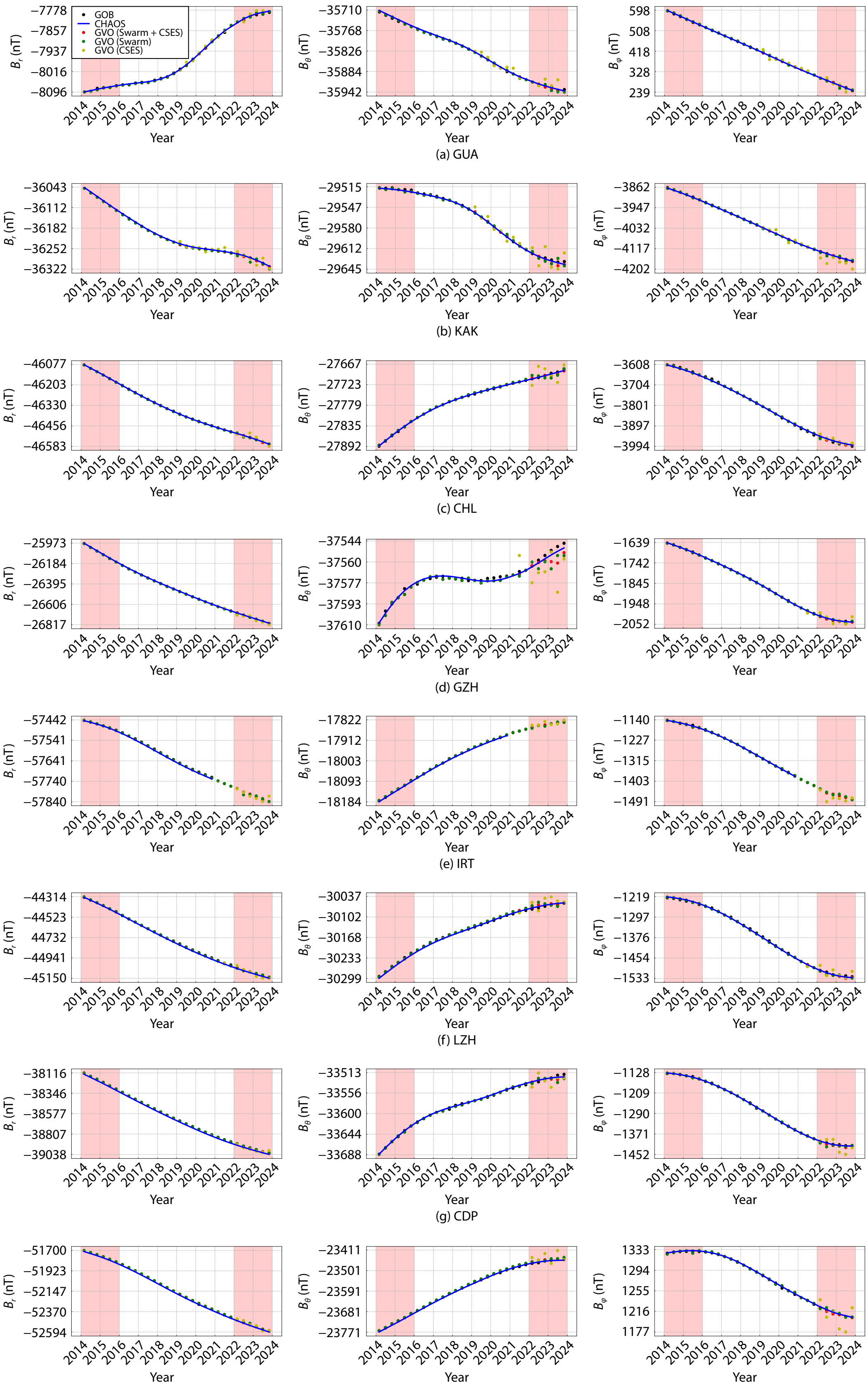

Figure 6. Four-monthly core field series: black dots are the GOB series, red dots are the GVO (Swarm+CSES) series, green dots are the GVO (Swarm) series, yellow dots are the GVO (CSES) series, blue line is the CHAOS series, red shaded areas represent the period of high solar activity. Each column from left to right is the B_r, B_θ and B_φ component.

that of the CHAOS model, while in the φ component, the highest accuracy of the GVO is 30% lower than that of the CHAOS model. For the four-monthly series, in both the r and θ components, the highest accuracy of the GVO are respectively 52% and 9% higher than that of the CHAOS model, while in the φ component, the highest accuracy of the GVO is 7% lower than that of the CHAOS model. In summary, for the core field series both in r and θ component, the accuracy of the GVO is higher than that of the CHAOS model, and lower than that of the CHAOS model in φ component. This discrepancy may be due to ionospheric or inter-hemispheric field-aligned currents. Additionally, there is a large deviation between the GVO and GOB series during the high solar activity period, especially in the horizontal component. Statistical calculations reveal that the RMSE for the one-monthly series during solar activity is about 30% higher than during quiet periods, while it is only about 17% higher for the four-monthly series.

In addition, we find strong consistency between the GVO series and model series. In the r, θ, and φ components, the accuracy are 2.15 nT, 2.13 nT and 1.16 nT, respectively. Although both of them are based on the Swarm satellite measurements, GVO additionally uses the CSES satellite measurements, and the methods used by both are completely independent. Therefore, GVO can be used to evaluate geomagnetic model accuracy. Another important finding from Tables 3 and 4 is that some observatories have relatively large RMSE, such as JYG, KSH, and CDP. By analyzing their series, two main reasons were found for the large RMSE: (1) during the stage of satellite payload adaptation and satellite orbit adjustment, the amount of data used for GVO method estimation is relatively small, resulting in imprecise estimations of GVO series; (2) ground observatories data, after undergoing baseline correction, may exhibit outliers at isolated time points, potentially attributed to instrument malfunction or observation inaccuracies.

Next we discuss the accuracy that the GVO (Swarm) and GVO (CSES) core field series can achieve. From Figures 5 and 6, it can be concluded that the results of GVO (Swarm) is close to the results of GVO (Swarm+CSES) and GOB series, whereas GVO (CSES) has a significant deviation and lower accuracy. At each ground observatory, we calculate the RMSE between them and the GOB and CHAOS series. Due to limitations of space, Table 5 only shows the average of the results.

As can be seen from the above Tables, for one-monthly series, GVO (Swarm+CSES) has improved accuracy by 10% (B_r), 19% (B_θ), and 8% (B_φ) respectively compared to GVO (Swarm), and by 73% (B_r), 76% (B_θ), and 79% (B_φ) respectively compared to GVO (CSES). For four-monthly series, GVO (Swarm+CSES) has improved accuracy by 6% (B_r), 21% (B_θ), and 11% (B_φ) respectively compared to GVO (Swarm), and by 76% (B_r), 83% (B_θ), and 86% (B_φ) respectively compared to GVO (CSES).

4.1.2 Accuracy of GVO series in secular variation

Although we have extended GVO series to the ground and removed local geomagnetic biases, a small gap still exists between the GVO and GOB series. To address this, the SV series can eliminate the small bias and more accurately evaluate the accuracy of the GVO method through the annual difference of monthly mean. Tables 6 and 7 present the results of validation comparisons with the ground observatories and core field model for the GVO SV series.

Tables 6 and 7 show that most RMSE in the GOB SV series are less than 3 nT/yr, indicating high consistency between two series. Additionally, the statistical results reveal that the accuracy of the radial component (B_r) are better than that of the horizontal component (B_θ and B_φ). This may be caused by the external current systems, such as Sq current system, equatorial electrojet, field-aligned currents, etc. Furthermore, the satellite operation region is in the ionospheric F-region, where in-situ electrical currents exist, whereas GVO estimation makes a potential field assumption, ignore the effect of the electrical currents, which can also cause some errors (Hammer et al., 2021).

Considering the measurement precision of Swarm and CSES, as well as the inherent measurement errors of the ground observatories, the highest accuracy the one-monthly and four-monthly GVO SV series can achieve is 2.03 nT/yr and 1.36 nT/yr, respectively. These numbers are considered as the upper accuracy limits for the GVO SV series estimations. Incomplete separation of the external signals affects the ground observatory and GVO series in different ways. The section "4.1.1 Accuracy of GVO series in core field", shows that GVO has higher accuracy than CHAOS in the r and θ component, but lower accuracy than CHAOS in the φ component. However, the results of Tables 6 and 7 show that GVO has lower

Table 5. Summary of comparisons for core field series between GVO (Swarm), GVO (CSES), GOB and CHAOS.

	GVO series	GOB			CHAOS		
		$RMSE_r$	$RMSE_\theta$	$RMSE_\varphi$	$RMSE_r$	$RMSE_\theta$	$RMSE_\varphi$
One-monthly GVO core field series (nT)	GVO (Swarm) mean	4.34	4.45	3.70	4.54	3.71	3.10
	GVO (Swarm) B-mean	3.35	3.58	2.59	3.12	3.38	2.36
	GVO (CSES) mean	11.79	11.93	11.40	12.02	11.42	11.20
	GVO (CSES) B-mean	11.22	10.55	9.51	10.38	10.39	9.19
Four-monthly GVO core field series (nT)	GVO (Swarm) mean	3.65	3.75	3.47	4.10	3.48	2.76
	GVO (Swarm) B-mean	2.87	2.94	2.52	3.48	2.75	2.12
	GVO (CSES) mean	12.85	14.70	16.09	13.29	14.57	15.44
	GVO (CSES) B-mean	11.30	14.01	15.62	12.40	14.04	14.66

Note：B-mean: the mean value of Benchmark observatories.

Table 6. Summary of comparisons for the one-monthly SV series.

	One-monthly SV series (nT/yr)								
	GVO vs GOB			CHAOS vs GOB			GVO vs CHAOS		
	$RMSE_r$	$RMSE_\theta$	$RMSE_\varphi$	$RMSE_r$	$RMSE_\theta$	$RMSE_\varphi$	$RMSE_r$	$RMSE_\theta$	$RMSE_\varphi$
NVS	2.08	2.56	1.79	1.99	2.23	1.56	1.60	1.55	2.02
IRT	2.23	2.57	2.50	1.88	2.18	1.54	1.88	1.60	2.35
MZL	2.51	2.82	2.22	1.91	1.99	1.52	1.29	2.21	1.61
KHB	1.63	2.50	2.11	1.72	2.22	2.21	1.10	1.58	1.41
WMQ	2.08	3.22	1.90	1.24	1.90	1.87	1.60	2.24	1.76
JYG	2.54	3.00	1.72	1.19	2.08	1.39	2.36	2.76	1.66
CHL	1.98	3.09	3.67	1.27	2.35	1.55	1.00	2.21	2.77
KSH	2.32	4.11	3.07	1.53	2.40	1.46	2.11	3.45	2.95
KAK	1.77	2.57	2.93	1.57	1.90	1.39	0.96	2.03	2.64
LZH	2.55	3.18	2.32	1.25	1.91	1.23	2.03	2.76	2.19
KNY	1.72	3.17	1.97	1.53	2.36	1.75	0.98	2.40	2.40
CDP	1.41	3.20	2.35	1.34	2.15	1.20	1.50	2.74	2.39
QZH	1.97	3.51	2.25	1.69	2.29	1.64	1.27	2.58	2.73
GZH	1.63	3.48	2.48	1.27	1.95	1.69	1.27	2.72	2.02
GUA	2.45	2.50	3.27	2.12	2.01	2.51	1.62	2.36	3.16
Mean	2.06	3.03	2.44	1.57	2.13	1.63	1.50	2.35	2.27
B-mean	2.03	2.79	2.44	1.56	1.99	1.60	1.48	1.96	2.25

Note：B-mean: the mean value of Benchmark observatories.

Table 7. Summary of Comparisons for the four-monthly SV series.

	Four-monthly SV series (nT/yr)								
	GVO vs GOB			CHAOS vs GOB			GVO vs CHAOS		
	$RMSE_r$	$RMSE_\theta$	$RMSE_\varphi$	$RMSE_r$	$RMSE_\theta$	$RMSE_\varphi$	$RMSE_r$	$RMSE_\theta$	$RMSE_\varphi$
NVS	2.99	2.55	1.20	1.44	1.55	3.06	3.07	1.89	1.04
IRT	1.36	1.65	1.85	1.28	1.87	2.94	1.60	1.93	2.06
MZL	1.55	3.22	1.81	1.27	2.62	3.01	1.10	1.58	2.07
KHB	1.59	1.36	1.90	1.49	1.73	4.73	1.14	0.91	1.52
WMQ	1.49	2.18	2.54	1.36	1.18	2.73	1.38	1.49	1.78
JYG	1.74	3.16	1.84	1.12	1.91	2.4	1.69	1.64	0.75
CHL	1.22	2.85	2.07	0.88	2.16	2.41	0.81	1.39	1.94
KSH	2.04	3.59	2.14	1.66	1.30	2.84	2.00	2.90	1.38
KAK	1.23	1.74	2.17	1.06	0.75	1.51	0.61	1.05	1.79
LZH	1.96	2.65	2.63	1.41	1.66	2.12	1.79	1.74	2.02
KNY	0.94	2.63	2.74	0.91	1.95	2.43	0.65	1.11	0.86
CDP	2.02	3.64	2.60	1.43	1.52	2.13	1.75	2.51	1.57
QZH	1.80	2.87	2.59	1.00	1.94	2.28	1.46	1.54	1.63
GZH	1.08	3.47	2.22	1.13	1.37	2.33	1.11	1.50	0.89
GUA	1.80	1.64	2.74	1.92	1.43	1.62	1.69	1.96	2.32
Mean	1.65	2.61	2.20	1.29	1.66	2.57	1.46	1.68	1.57
B-mean	1.36	1.86	2.19	1.23	1.27	2.39	1.20	1.49	1.88

Note：B-mean: the mean value of Benchmark observatories.

accuracy than CHAOS in all components. This is because the core field series has not undergone any smoothing process, and has some small fluctuations. The SV series is obtained through difference, which amplifies these small fluctuations. Although GVO's accuracy is lower than that of CHAOS, its ability to capture the SV trend is equivalent to that of CHAOS.

Figures 7 and 8 present the SV series of the GVO, GOB and CHAOS model, both the amplitude and trend of the GVO (Swarm+CSES) and GVO (Swarm) SV series are well matched to the GOB SV series. The GVO (CSES) has a large deviation and poor accuracy, and so it is impossible to reflect true amplitude and trend of SV. The results of the SV series also indicate that radical component (B_r) has the highest accuracy, while the horizontal component (B_θ and B_φ) has lower accuracy. The SV series of southward θ component and eastward φ component have larger fluctuations and external noise; 4-monthly SV series can better eliminate external noise and obtain more accurate results.

A jerk is the sudden change phenomenon in the SV series. Its main feature is the "∧" or "∨" shape in the SV series, and as the step changes "/" or "\" shape centered on zero in the SA series (Mandea et al., 2010). The GVO SV series captures this important rapid temporal feature very well. For example, the 2017 jerk and 2020 jerk, one year before or after them, can be observed clearly at the above observatories; the four-monthly SV series may lose some temporal resolution. There is a shortcoming in calculating the time and intensity of jerk occurrence using only the CHAOS series, and adding the GVO series can improve this deficiency. In conclusion, the GVO series can provide the same significant temporal resolution as the GOB series.

As can be seen from Table 8, for the one-monthly series, GVO (Swarm+CSES) has improved accuracy by 19%, 10%, and 4% compared to GVO (Swarm) in the , θ, and φ component, respectively. And for the four-monthly series, GVO (Swarm+CSES) has improved accuracy by 58%, 22%, and 37%. Because the GVO (CSES) series cannot reflect the true information of SV, its RMSE has no practical significance, so we do not calculate the accuracy improvement of GVO (Swarm+CSES) by comparison.

5. Discussion and Conclusions

We apply the GVO method to derive the series of geomagnetic core field and its SV for the ground observatory. As shown in Tables 3 and 4, we find that one-monthly and four-monthly GVO core field series can reach the highest accuracy of 2.24 nT and 1.16 nT respectively, and one-monthly and four-monthly GVO SV series can reach the highest accuracy of 2.03 nT/yr and 1.36 nT/yr, respectively. These results indicate that the GVO products match well with independent ground observatories, and their precision meet the INTERMAGNET standards for quasi-definitive data. Therefore, the GVO products provide consistent and accurate observation of the geomagnetic core field and its SV.

In one-monthly core field series, GVO (Swarm+CSES) improves accuracy by about 0.4 nT compared to GVO (Swarm), and about 7.5 nT compared to GVO (CSES). In four-monthly core field series, GVO (Swarm+CSES) respectively improves accuracy by about 0.4 nT and 11 nT. Compared to GVO (CSES), GVO (Swarm) has significantly improved evaluation accuracy. There are two main reasons for the poor accuracy of GVO (CSES): (1) there are few CSES data used for GVO fitting in each period, and the data accuracy is lower than Swarm; (2) CSES has only one satellite, and only the differences and sums of along-track participate in the GVO fitting process, resulting in the loss of some information of the core field.

Compared to the GOB SV series, GVO SV series can match them well in terms of the amplitude of secular variation and secular acceleration. Jerks are captured well and there is no indication of loss of temporal resolution. In the GVO series, the error in the horizontal component is larger than in the vertical component, especially the θ component which has the largest error. The amplitude of this error deviation is somewhat related to the level of solar activity. In one and four-monthly SV series, GVO (Swarm+CSES) respectively improve accuracy by about 0.3 nT/yr and 1.2 nT/yr compared to GVO (Swarm). This study demonstrates that GVO method is a useful and effective way to extract geomagnetic core field, which can be adjusted according to research interests.

In this study, we use conditions such as geomagnetic index to eliminate data that is affected by external field interference, which greatly reduces the amount of data used for the GVO method. Therefore, we need to establish an external field model with high precision and high spatiotemporal resolution to remove external signals. In addition, we use the PCA denoising based on the annual difference of the monthly GVO series. For future work, we should use more detailed denoising methods to reduce evaluation errors in the horizontal component. Some studies have already used the GVO products in inversions of the core surface flow (Kloss and Finlay, 2019), the core signals from GVO products and other geophysical field signals are combined together to estimate the variation state of the core more accurately. Furthermore, MSS-1 was launched in 2023, which is the world's first low-inclination geomagnetic satellite mission (Yan Q and Yao HB, 2024), and CSES2 was launched in 2023, which observation range can cover the global earth compared to CSES1 (Zeren ZM et al., 2023). The constellation mission could also provide high-precision geomagnetic observations. We can use improving multi-source satellite geomagnetic measurements for more accurate assessment of the geomagnetic field based on the GVO method.

Acknowledgments

This study is supported by the Special Fund of the Institute of Geophysics, China Earthquake Administration (grant no. DQJB24X25). Swarm satellite data are available from https://earth.esa.int/web/guest/swarm/data-access. CSES satellite data can be accessed at https://leos.ac.cn/#/dataService/dataDownloadList. The RC index is available from https://www.spacecenter.dk/files/magnetic-models/RC/. The CHAOS model is available from http://www.spackcenter.dk/files/magnetic-models/CHAOS-7/. Ground observatory data are available from INTERMAGNET and China Earthquake Networks Center. *Kp*, *Dst*, and Q-days data are available from the World Data Center for Geomagnetism, Kyoto. The OMNI data are available from the GSFC/SPDF OMNIWeb interface at https://omniweb.gsfc.nasa.gov/ow.html. We thank Professor Chris Finlay from Technical University of Denmark and Dr

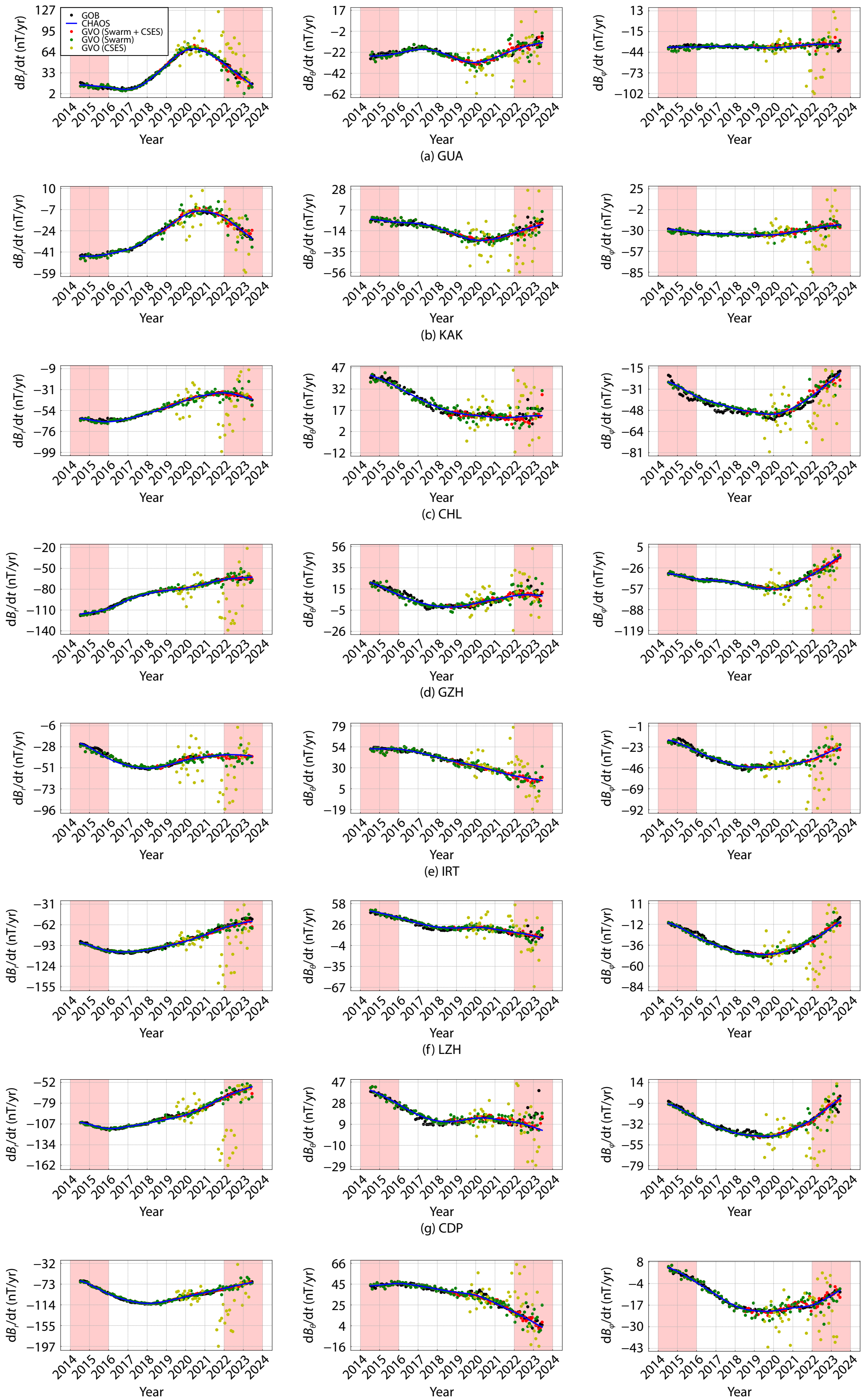

Figure 7. One-monthly SV series: black dots are the GOB series, red dots are the GVO (Swarm+CSES) series, green dots are the GVO (Swarm) series, yellow dots are the GVO (CSES) series, blue line is the CHAOS series, red shaded areas represent the period of high solar activity. Each column from left to right is the B_r, B_θ and B_φ component.

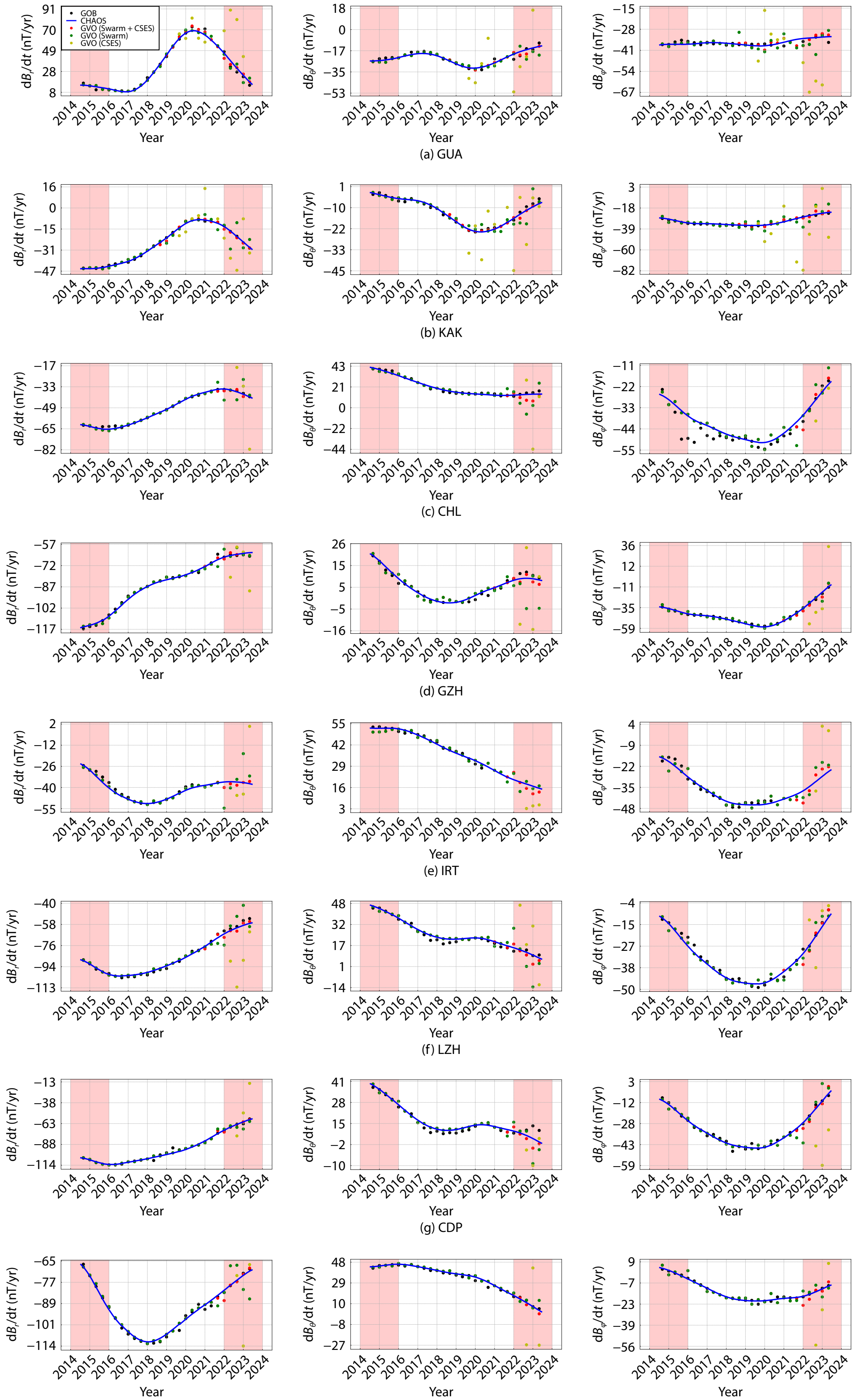

Figure 8. Four-monthly SV series: black dots are the GOB series, red dots are the GVO (Swarm+CSES) series, green dots are the GVO (Swarm) series, yellow dots are the GVO (CSES) series, blue line is the CHAOS series, red shaded areas represent the period of high solar activity. Each column from left to right is the B_r, B_θ and B_φ component.

Table 8. Summary of comparisons for SV series between GVO (Swarm), GVO (CSES), GOB and CHAOS.

GVO series		GOB			CHAOS		
		$RMSE_r$	$RMSE_\theta$	$RMSE_\varphi$	$RMSE_r$	$RMSE_\theta$	$RMSE_\varphi$
One-monthly GVO SV series (nT/yr)	GVO (Swarm) mean	3.55	4.11	3.63	3.44	3.96	3.39
	GVO (Swarm) B-mean	2.50	3.09	2.35	3.39	3.78	3.36
	GVO (CSES) mean	27.95	17.25	20.07	28.79	19.35	21.64
	GVO (CSES) B-mean	22.80	17.04	14.62	25.91	17.78	19.35
Four-monthly GVO SV series (nT/yr)	GVO (Swarm) mean	3.47	4.36	4.00	4.66	3.69	3.81
	GVO (Swarm) B-mean	3.27	2.39	3.47	3.12	2.36	3.45
	GVO (CSES) mean	21.40	24.58	26.71	20.77	20.08	25.42
	GVO (CSES) B-mean	19.21	20.48	20.68	20.31	20.02	20.69

B-mean: the mean value of Benchmark observatories.

William Brown from British Geological Survey for providing sample code and answering my questions.

References

Alexandrescu, M., Gibert, D., Hulot, G., Le Mouël, J. L., and Saracco, G. (1996). Worldwide wavelet analysis of geomagnetic jerks. *J. Geophys. Res.: Solid Earth*, *101*(B10), 21975–21994. https://doi.org/10.1029/96JB01648

Backus, G., Parker, R., and Constable, C. (1996). *Foundations of Geomagnetism*. Cambridge, New York: Cambridge University Press.

Bai, C. H., Gao, G. M., Wen, L. M., and Kang, G. F. (2024). Dynamic evolution of amplitude and position of geomagnetic secular acceleration pulses since 2000. *Front. Earth Sci.*, *12*, 1383149. https://doi.org/10.3389/feart.2024.1383149

Barrois, O., Hammer, M. D., Finlay, C. C., Martin, Y., and Gillet, N. (2018). Assimilation of ground and satellite magnetic measurements: inference of core surface magnetic and velocity field changes. *Geophys. J. Int.*, *215*(1), 695–712. https://doi.org/10.1093/gji/ggy297

Beggan, C. D., Whaler, K. A., and Macmillan, S. (2009). Biased residuals of core flow models from satellite-derived 'virtual observatories'. *Geophys. J. Int.*, *177*(2), 463–475. https://doi.org/10.1111/j.1365-246X.2009.04111.x

Beggan, C. D., Macmillan, S., Hamilton, B., and Thomson, A. W. P. (2013). Independent validation of Swarm Level 2 magnetic field products and 'Quick Look' for Level 1b data. *Earth, Planets Space, 65*(11), 1345–1353. https://doi.org/10.5047/eps.2013.08.004

Brown, W. J., Mound, J. E., and Livermore, P. W. (2013). Jerks abound: An analysis of geomagnetic observatory data from 1957 to 2008. *Phys. Earth Planet. Inter.*, *223*, 62–76. https://doi.org/10.1016/j.pepi.2013.06.001

Campuzano, S. A., Pavón-Carrasco, F. J., De Santis, A., González-López, A., and Qamili, E. (2021). South Atlantic anomaly areal extent as a possible indicator of geomagnetic jerks in the satellite era. *Front. Earth Sci.*, *8*, 607049. https://doi.org/10.3389/feart.2020.607049

Chulliat, A., and Maus, S. (2014). Geomagnetic secular acceleration, jerks, and a localized standing wave at the core surface from 2000 to 2010. *J. Geophys. Res.: Solid Earth*, *119*(3), 1531–1543. https://doi.org/10.1002/2013JB010604

Cox, G., Brown, W., Beggan, C., Hammer, M., and Finlay, C. (2020). Deonising Swarm Geomagnetic Virtual Observatories using principal component analysis. EGU General Assembly 2020, Online, 4-8 May 2020, EGU2020-9957. https://doi.org/10.5194/egusphere-egu2020-9957

Cox, G. A., Brown, W. J., Billingham, L., and Holme, R. (2018). MagPySV: A python package for processing and denoising geomagnetic observatory data. *Geochem. Geophys. Geosyst., 19*(9), 3347–3363. https://doi.org/10.1029/2018GC007714

Domingos, J., Pais, M. A., Jault, D., and Mandea, M. (2019). Temporal resolution of internal magnetic field modes from satellite data. *Earth, Planets Space, 71*, 2. https://doi.org/10.1186/s40623-018-0983-5

Finlay, C. C., Kloss, C., Olsen, N., Hammer, M. D., TΦffner-Clausen, L., Grayver, A., and Kuvshinov, A. (2020). The CHAOS-7 geomagnetic field model and observed changes in the South Atlantic Anomaly. *Earth, Planets Space, 72*(1), 156. https://doi.org/10.1186/s40623-020-01252-9

Friis-Christensen, E., Finlay, C. C., Hesse, M., and Laundal, K. M. (2017). Magnetic field perturbations from currents in the dark polar regions during quiet geomagnetic conditions. *Space Sci. Rev.*, *206*(1), 281–297. https://doi.org/10.1007/s11214-017-0332-1

Hammer, M. D. (2018). *Local Estimation of the Earth's Core Magnetic Field*. Copenhagen: Technical University of Denmark.

Hammer, M. D., Cox, G. A., Brown, W. J., Beggan, C. D., and Finlay, C. C. (2021). Geomagnetic Virtual Observatories: monitoring geomagnetic secular variation with the Swarm satellites. *Earth, Planets Space, 73*, 54. https://doi.org/10.1186/s40623-021-01357-9

Hammer, M. D., Finlay, C. C., and Olsen, N. (2022). Secular variation signals in magnetic field gradient tensor elements derived from satellite-based geomagnetic virtual observatories. *Geophys. J. Int.*, *229*(3), 2096–2114. https://doi.org/10.1093/gji/ggac004

Huder, L., Gillet, N., Finlay, C. C., Hammer, M. D., and Tchoungui, H. (2020). COV-OBS.x2: 180 years of geomagnetic field evolution from ground-based and satellite observations. *Earth, Planets Space, 72*(1), 160. https://doi.org/10.1186/s40623-020-01194-2

Khanyile, S. L., and Nahayo, E. (2024). Geomagnetic jerks observed in geomagnetic observatory data over southern Africa between 2017 and 2023. *South Afr. J. Geol.*, *127*(1), 131–136. https://doi.org/10.25131/sajg.127.0019

Kim, H. R., and von Frese, R. R. B. (2013). Localized analysis of polar geomagnetic jerks. *Tectonophysics*, *585*, 26–33. https://doi.org/10.1016/j.tecto.2012.06.038

Kloss, C., and Finlay, C. C. (2019). Time-dependent low-latitude core flow and geomagnetic field acceleration pulses. *Geophys. J. Int.*, *217*(1), 140–168. https://doi.org/10.1093/gji/ggy545

Kotsiaros, S., Finlay, C. C., and Olsen, N. (2015). Use of along-track magnetic field differences in lithospheric field modelling. *Geophys. J. Int.*, *200*(2), 880–889. https://doi.org/10.1093/gji/ggu431

Kotsiaros, S. (2016). Toward more complete magnetic gradiometry with the Swarm mission. *Earth, Planets Space, 68*, 130. https://doi.org/10.1186/s40623-016-0498-x

Li, Y. J., Feng, Y., Zhang, S. Q., Liu, S., Zhang, J. Y., and Wei, G. C. (2023). The study of geomagnetic jerk from 2010 to 2021 based on hourly mean data from global geomagnetic observatories. *Earth Planet. Phys.*, *7*(1), 39–48. https://doi.org/10.26464/epp2023016

Lu, S. K., Zhang, H., Li, X. H., Liu, D. Z., and Wang, X. Q. (2016). Empirical evidence for latitude dependence and asymmetry of geomagnetic spatial variation in mainland China. *Geophys. Res. Lett.*, *43*(9), 4350–4357. https://doi.org/10.1002/2016GL068345

Macmillan, S., and Olsen, N. (2013). Observatory data and the Swarm mission. *Earth, Planets Space, 65*(11), 1355–1362.

https://doi.org/10.5047/eps.2013.07.011

Mandea, M., and Olsen, N. (2006). A new approach to directly determine the secular variation from magnetic satellite observations. *Geophys. Res. Lett.*, *33*(15), L15306. https://doi.org/10.1029/2006GL026616

Mandea, M., Holme, R., Pais, A., Pinheiro, K., Jackson, A., and Verbanac, G. (2010). Geomagnetic jerks: Rapid core field variations and core dynamics. *Space Sci. Rev.*, *155*(1-4), 147–175. https://doi.org/10.1007/s11214-010-9663-x

Olsen, N., and Mandea, M. (2007). Investigation of a secular variation impulse using satellite data: The 2003 geomagnetic jerk. *Earth Planet Sci. Lett.*, *255*(1-2), 94–105. https://doi.org/10.1016/j.epsl.2006.12.008

Olsen, N., and Mandea, M. (2008). Rapidly changing flows in the Earth's core. *Nat. Geosci.*, *1*(6), 390–394. https://doi.org/10.1038/ngeo203

Olsen, N., Mandea, M., Sabaka, T. J., and TΦffner-Clausen, L. (2009). CHAOS-2—a geomagnetic field model derived from one decade of continuous satellite data. *Geophys. J. Int.*, *179*(3), 1477–1487. https://doi.org/10.1111/j.1365-246X.2009.04386.x

Olsen, N., Lühr, H., Finlay, C. C., Sabaka, T. J., Michaelis, I., Rauberg, J., and TΦffner-Clausen, L. (2014). The CHAOS-4 geomagnetic field model. *Geophys. J. Int.*, *197*(2), 815–827. https://doi.org/10.1093/gji/ggu033

Olsen, N., Hulot, G., Lesur, V., Finlay, C. C., Beggan, C., Chulliat, A., Sabaka, T. J., Floberghagen, R., Friis-Christensen, E. … Vigneron, P. (2015). The Swarm Initial Field Model for the 2014 geomagnetic field. *Geophys. Res. Lett.*, *42*(4), 1092–1098. https://doi.org/10.1002/2014GL062659

Olsen, N., Ravat, D., Finlay, C. C., and Kother, L. K. (2017). LCS-1: A high-resolution global model of the lithospheric magnetic field derived from CHAMP and *Swarm* satellite observations. *Geophys. J. Int.*, *211*(3), 1461–1477. https://doi.org/10.1093/gji/ggx381

Pavón-Carrasco, F. J., Marsal, S., Campuzano, S. A., and Torta, J. M. (2021). Signs of a new geomagnetic jerk between 2019 and 2020 from *Swarm* and observatory data. *Earth, Planets Space, 73*, 175. https://doi.org/10.1186/s40623-021-01504-2

Qamili, E., De Santis, A., Isac, A., Mandea, M., Duka, B., and Simonyan, A. (2013). Geomagnetic jerks as chaotic fluctuations of the Earth's magnetic field. *Geochem., Geophys., Geosyst., 14*(4), 839–850. https://doi.org/10.1029/2012GC004398

Rogers, H. F., Beggan, C. D., and Whaler, K. A. (2019). Investigation of regional variation in core flow models using spherical Slepian functions. *Earth, Planets Space*, 71, 19. https://doi.org/10.1186/s40623-019-0997-7

Sabaka, T. J., TΦffner-Clausen, L., and Olsen, N. (2013). Use of the Comprehensive Inversion method for *Swarm* satellite data analysis. *Earth, Planets Space, 65*(11), 1201–1222. https://doi.org/10.5047/eps.2013.09.007

Sabaka, T. J., TΦffner-Clausen, L., Olsen, N., and Finlay, C. C. (2018). A comprehensive model of Earth's magnetic field determined from 4 years of Swarm satellite observations. *Earth, Planets Space, 70*(1), 130. https://doi.org/10.1186/s40623-018-0896-3

Shen, X. H., Zhang, X. M., Yuan, S. G., Wang, L. W., Cao, J. B., Huang, J. P., Zhu, X. H., Piergiorgio, P., and Dai, J. P. (2018). The state-of-the-art of the China Seismo-Electromagnetic Satellite mission. *Sci. China Technol. Sci.*, *61*(5), 634–642. https://doi.org/10.1007/s11431-018-9242-0

Shore, R. M. (2013). *Improved Description of Earth's External Magnetic Fields and Their Source Regions Using Satellite Data*. Edinburgh: The University of Edinburgh.

Torta, J. M., Pavón-Carrasco, F. J., Marsal, S., and Finlay, C. C. (2015). Evidence for a new geomagnetic jerk in 2014. *Geophys. Res. Lett.*, *42*(19), 7933–7940. https://doi.org/10.1002/2015GL065501

Yan, Q., and Yao, H. B. (2024). Recent geomagnetic storms observed by Macau Science Satellite-1. *Earth Planet. Phys.*, *8*(4), 565–569. https://doi.org/10.26464/epp2024047

Yang, Y. Y., Zhou, B., Hulot, G., Olsen, N., Wu, Y. Y., Xiong, C., Stolle, C., Zhima, Z., Huang, J. P. … Shen, X. H. (2021). CSES high precision magnetometer data products and example study of an intense geomagnetic storm. *J. Geophys. Res.: Space Phys.*, *126*(4), e2020JA028026. https://doi.org/10.1029/2020JA028026

Zeren, Z. M., Liu, D. P., Sun, X. Y., Yang, Y. Y., Zhao, S. F., Yan, R., Zhang, Z. X., Huang, H., Yang, D. H. … Shen, X. H. (2023). Current status and scientific progress of the Zhangheng-1 satellite mission. *Reviews of Geophysics and Planetary Physics* (in Chinese), *54*(4), 455–465. https://doi.org/10.19975/j.dqyxx.2022-043